Energy transfer in ion−Rydberg-atom charge exchange

D. S. Fisher and S. R. Lundeen

Department of Physics, Colorado State University, Fort Collins, Colorado 80523

C. W. Fehrenbach and B. D. DePaola

Department of Physics, Kansas State University, Manhattan, Kansas 66506

(Received 27 October 2000; published 17 April 2001)

Charge-transfer collisions between slow multiply charged ions and highly excited Rydberg atoms have been studied to determine the details of the internal energy transfer accompanying charge exchange. The experiment uses lasers to define uniquely the binding energies of both initial and final states of the collision, thereby eliminating the ambiguity inherent in the selective field ionization method used for previous studies. The results clearly characterize the capture energetics over the range of ion charge $q = 1-11$ and velocity $v = 0.031-0.138$ a.u. The measurements are in very good agreement with predictions of the classical trajectory Monte Carlo method, but not with predictions of other classical models.

INTRODUCTION

The charge-exchange reaction between multiply charged ions and highly excited atoms occurs with very large cross sections and results in highly excited products within a narrow range of energies. For example, a slow bare oxygen nucleus can capture an electron from a hydrogen atom in the $n = 14$ state with a cross section of about one square micron, and will likely result in an $n = 80$ state of hydrogenic oxygen, lying 870 eV above the ground state of that system. This is potentially an important cooling mechanism in hot plasmas, since such a product state may decay radiatively, releasing almost 1 keV of energy in the form of photons for each charge capture. Of course the tendency to form highly excited products is also present in collisions of multiply charged ions with atomic ground states, but the very large capture cross sections for highly excited states gives them importance beyond their relative abundance. An additional reason for interest in the ion–Rydberg-atom charge-transfer collisions is that they result in controllable, highly inverted populations in the product ions. These could be useful in some schemes to produce x-ray lasers or in the study of other processes involving excited states.

Because of the very large number of quantum states involved when the target atom is highly excited, there have been no successful quantum-mechanical treatments of these collisions. To date, the most successful theoretical description is obtained with classical mechanics. The classical trajectory Monte Carlo (CTMC) method treats the collision as a three-body classical problem [1]. An initial classical orbit for the target electron is selected randomly from a distribution representing all possible orientations and orbital phases of elliptical orbits whose energy and angular momentum lie within a discrete range corresponding to the quantum numbers of the target. The incident ion's velocity and impact parameter are chosen, and the classical equations of motion are integrated through the collision. When the heavy particles are well separated, if the electron is bound to the projectile ion, its energy and angular momentum relative to the ion are determined and used to infer its ''quantum state,''

using the same discrete correspondence as for the initial state. To what extent this theoretical approach gives an adequate description of ion–Rydberg-atom charge transfer is still an open question. In a broader sense, these collisions provide an interesting case for studying the classical-quantum correspondence. Characteristic quantum features known to be important in ground-state collisions, such as level anticrossings, do not occur in classical treatments, but may possibly appear in another guise.

Despite the fascinating characteristics of ion–Rydberg-atom collisions, there have been very few experimental studies of their properties. MacAdam, Gray, and Rolfes pioneered this field, using slow beams of Na^+ ions incident on excited Na targets [2]. In these studies, the product states were analyzed using selective field ionization. Later, Pesnelle used a similar approach to study the results of collisions between Kr^{8+} ions and a target of excited Rb atoms [3]. In both cases, the experiments confirmed the predicted resonant nature of the capture, i.e., the tendency to populate a narrow range of product states with binding energies approximately equal to that of the target electron. However, important details of the experimental results, such as the most probable final-state energy and the width of the final-state energy distribution, appeared to differ significantly from the predictions of the CTMC method in both experiments. Part of the problem could lie in the method of analysis of the product states. The selective field ionization (SFI) method assumes a unique correspondence between the binding energy of a state and the electric field leading to its Stark ionization. While this is approximately true, the actual field that ionizes excited atoms of a fixed principal quantum number can vary by as much as a factor of 3, depending on the other quantum numbers of the state and the slew rate of the ionizing field [4].

In view of the ambiguity inherent in the SFI method, a more quantitative approach is needed to achieve a definitive test of CTMC predictions for this process. One possible approach was first demonstrated in 1993 in Ref. [5]. In this experiment, a beam of S^+ ions captured an electron from a Rydberg-atom target of Rb. Following the charge capture,

particular product states were selectively detected by laser excitation upward to a very weakly bound discrete state, followed by Stark ionization of this state and collection of the resulting current. We now refer to this method of detection as resonant excitation Stark ionization spectroscopy (RESIS). This is a sensitive and selective way to detect specific excited states. Using a Doppler-tuned CO_2 laser, it can easily detect neutral Rydberg states with principal quantum numbers $n = 9$ or 10, and in favorable cases fully resolve the fine structure of these states. For example, in Ref. [5] all the $n = 10$ fine-structure levels with $L \geq 4$ were fully resolved in the RESIS spectrum. Using this method, the authors of Ref. [5] demonstrated that the populations of the various L levels within $n = 9$ and 10 manifolds were dramatically nonstatistical, and that this distribution changed noticeably when the excitation level of the Rydberg-atom target was changed from 8 to 10 [5]. Unfortunately, this study yielded only fragmentary information regarding the energy distributions following charge capture, because the RESIS method cannot easily be applied to detect energy levels other than 9 and 10.

A way to surmount this difficulty and use the RESIS method to study the energy distributions was first demonstrated by Fisher *et al.* in 1997 [6]. In this study, the characteristics of the resonant capture were revealed not by studying the populations of a range of final states produced from a fixed energy initial state, but instead by studying the population of a fixed-energy final state as the energy of the initial Rydberg-atom target state was varied. While somewhat indirect, this approach retains the advantages of uniquely defined energies in both the initial and final states, and is in this sense an improvement over the SFI method. In this study, He^+ ions were incident on a Rydberg target with a principal quantum number n_t that could be tuned over the range $7 \leq n_t \leq 14$. The RESIS signals corresponding to excitation from $n_L = 10$ to $n_U = 30$ were measured, with $L = 4$ and 5 states resolved and highest L levels, $L = 7-9$ forming an unresolved high-L peak. The strength of these RESIS signals is proportional to the population in these specific states. Tuning the excitation level of the Rydberg target should reveal which target produces these levels most efficiently. Since targets with different values of n_t may have different thicknesses, the total charge-transfer beam, in this case neutral helium, was also measured. The ratio of the RESIS signal to the total charge-transfer beam is independent of the target thickness. Measurements of this ratio vs n_t show a characteristic variation which depends on the details of the energy distribution in charge capture. The results of Fisher *et al.* were consistent with the energy distributions predicted by the CTMC method over this range of target energies. Limited information was also obtained about the L distributions, which did not agree as well with CTMC predictions.

The RESIS method was extended to multiply-charged ions in a second study by Fisher *et al.* [7]. Using ions with charge $q = 2$, 3, and 4, and at a range of velocities, this study used the same indirect method of probing the energy transfer used earlier for singly charged ions [6]. In this case, the RESIS transitions used to detect particular final states of Rydberg ions were $q = 2(19-51)$, $q = 3(29-71)$, and $q = 4(37-85)$. The Rydberg target was tuned over the range
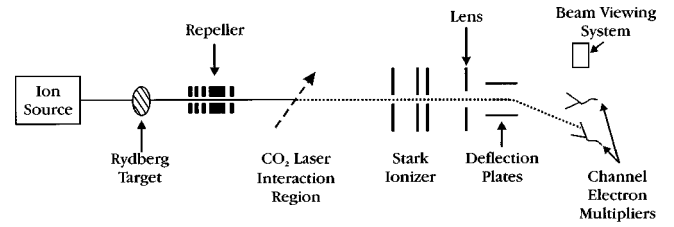
FIG. 1. Schematic diagram of the apparatus used for this study. A beam of multiply charged ions passes through the Rydberg-atom target, where some fraction captures single electrons to form highly excited Rydberg ions. Along with the residual primary ion beam, these ions enter the repeller. There, the primary ion beam is blocked, while the charge transfer beam of Rydberg ions is transmitted and refocused. The electric fields in the repeller also Stark ionize very highly excited levels that could otherwise contribute to background in the detector. Following this, a Doppler-tuned CO_2 laser excites Rydberg ions from a specific energy state (n_L) to a very highly excited level (n_U). Ions excited to the n_U level are subsequently Stark ionized in the detector, focused, and deflected into a channel electron multiplier (CEM). A beam-viewing system mounted opposite the CEM is used to visualize the beam, while the lens voltage is adjusted. The primary measured quantity is the ratio between the CO_2-induced signal and the total charge-transfer current.

$7 \leq n_t \leq 18$. In each case, the strength of the high-L RESIS signal was measured to indicate the population of the lower n-level. As in Ref. [6], the total charge-transfer beam was also measured, and the ratio of these two measured quantities was compared to theory. The results clearly showed that, for $q > 1$, the final state was more tightly bound than the target state which produced it most efficiently. However the size of this shift appeared to be in disagreement with CTMC calculations. The width of the capture resonance was also shown to vary systematically with the charge and velocity of the incident ion.

This paper reports an extended and improved version of the experiment described in Ref. [6]. The range of ion charges and velocities has been extended, and additionally a wider range of target energies has been obtained to more fully define the capture resonances. The measurements are compared to CTMC predictions, incorporating several systematic corrections omitted in Ref. [6]. This removes the apparent discrepancy with CTMC predictions reported there. The final results reported here agree very well with CTMC predictions over the entire range of charges and velocities studied. This full report gives detailed descriptions of the apparatus used for this study, and of the various systematic corrections applied in comparison with the CTMC method. Also included is a more complete description of the operation of the Rydberg-atom target. Some of the features of its operation are not yet understood and merit further study, but these remaining questions do not interfere with its use in this application.

APPARATUS

Figure 1 shows a schematic diagram of the apparatus used

TABLE I. Specific ions used for this study. All have $L=0$ ground states. The last column gives the dipole polarizability used to calculate the fine structure in the detected levels.

Charge	Ion	Velocity (a.u.)	K. E. (eV)	α_d (units of a_0^3)
1	$^4He^+$	0.100	1000	$9/32$[a]
2	$^{13}C^{2+}$	0.100	3250	3.56[b]
3	$^{13}C^{3+}$	0.100	3250	4.0[b]
4	$^{13}C^{4+}$	0.100	3250	0.009[c]
6	$^{22}Ne^{6+}$	0.100	5500	0.428[d]
8	$^{40}Ar^{8+}$	0.100	10 000	0.062[b]
11	$^{40}Ar^{11+}$	0.100	10 000	0.019[b]
3	$^{133}Xe^{3+}$	0.031	3195	10.25[d]
3	$^{40}Ar^{3+}$	0.043	1850	3.52[d]
3	$^{40}Ar^{3+}$	0.057	3250	3.52[d]
3	$^{13}C^{3+}$	0.081	2132	4.0[b]
3	$^{13}C^{3+}$	0.130	5492	4.0[b]

[a]Dalgarno and Lewis [23].
[b]Estimated.
[c]Bhatia and Drachman [25].
[d]Charlotte Fischer (private communication) [24].

for these measurements. It is very similar to that used for the studies of singly charged ions [6]. The major difference is that in place of the electric deflection field following the Rydberg-atom target, this apparatus has a double electrostatic lens which functions as a ''repeller.'' A brief description of the various elements is given in the caption of Fig. 1. The critical distance scales are as follows:

(1) Rydberg-atom target to repeller center: 23 cm.
(2) Repeller center to CO_2 laser: 22 cm.
(3) CO_2 laser to Stark ionizer: 35 cm.

The ion beams were produced by the CryEBIS ion source at the J.R. Macdonald Laboratory at Kansas State University [8]. Ions were chosen whose ground electronic states were S states, in order to insure a relatively simple heliumlike Rydberg fine structure. Working under the assumption that the presence of tightly bound core electrons is irrelevant in collisions with highly excited Rydberg states, it was convenient to use ions of different mass to vary the beam velocity. With this choice, many of the electrostatic focusing elements could be left virtually unchanged as the velocity varied. Table I [23–25] shows the specific ions used.

The Ryberg-atom target used here is the same device used in previous experiments [5,6,7]. It consists of a thermal Rb beam, excited by three cw lasers to the $n_t F_{7/2}$ state where $7 \leq n_t \leq 26$. The more abundant isotope, ^{85}Rb, is excited in the sequence of transitions (1) $5S_{1/2}(F=3)$ to $5P_{3/2}(F=4)$ at 780 nm, (2) $5P_{3/2}(F=4)$ to $4D_{5/2}(F=5)$ at 1529 nm, and (3) $4D_{5/2}(F=5)$ to $n_t F_{7/2}(F=6)$ at $\lambda(n_t)$. The range of targets used for this study includes $n_t = 7-18$, 20, 22, and 26. This gives a range of target binding energies ranging from 0.278 to 0.020 eV. The wavelength of the final transition, $\lambda(n_t)$, varies from 827 to 705 nm. The transition energies for
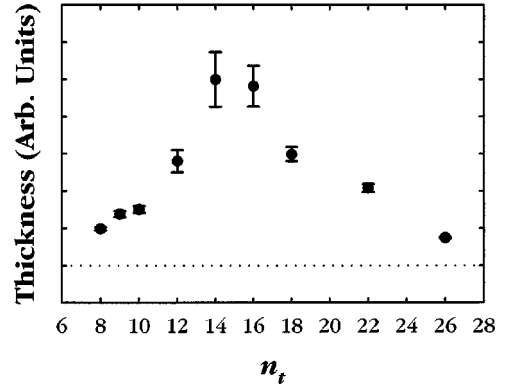
FIG. 2. Relative values of the target thickness for several Rydberg-atom targets of different binding energies. The horizontal axis gives the principal quantum number of the $F_{7/2}$ state excited by the third laser. The vertical axis is an estimate of the target thickness, obtained by dividing the total charge-transfer current by the calculated total charge-transfer cross section. The variation is due, in part, to the variation of the third laser power as its frequency is tuned between 705 and 826 nm.

these transitions were measured with precision of about 0.02 cm^{-1}, and were found to be given approximately by the expression

$$E(n_t F_{7/2}) - E(4D_{5/2}) \cong 14\,335.50 - \frac{109\,736.63}{(n_t - 0.0150)^2}\,cm^{-1}.$$

(1)

The spectral width of the excitation lasers was <30 MHz, and the observed linewidth of the excitation transitions was on the order of 100 MHz. The total excited-state density present in the several Rydberg-atom targets was estimated by comparing the size of the charge-transfer beam obtained with each target, and dividing by the calculated total charge-transfer cross section for each target. The results, shown in Fig. 2, indicate that the total density is maximum for around $n_t = 14$, and decreases by about an order of magnitude at $n_t = 7$ or 26. These are only typical results, obtained during a single day. From day to day, the actual target thickness can vary depending on the conditions of the Rb oven and the excitation lasers. We estimate that the peak target density corresponds to about 3×10^8 excited atoms within an approximately spherical volume of radius 3 mm, giving a peak density of approximately 3×10^9 excited atoms/cm^3. In this experiment, since the measured quantity is the ratio of the RESIS signal to the charge-transfer beam, and, since both of these quantities are proportional to the total target thickness, the absolute target thickness should not affect the result. This is true as long as the charge transfer associated with the lower states of Rb ($5S$, $5P$, and $4D$) is negligible compared with the charge transfer from the target's final state $(n_t F, (n_t + 1)D)$. From previous studies [9], it can be shown that the total charge-transfer beam from these lower states is negligible in this experiment.

Although the lasers excite only the $n_t F_{7/2}$ level, this population is efficiently shared with the nearby $(n_t + 1)D_{5/2}$ level. The mechanism for this population sharing has been de-

scribed as a ''mirrorless maser,'' and was discussed elsewhere [10]. Briefly, the population inversion created by excitation of the $n_tF_{7/2}$ level creates large gain on the far-infrared transition from $n_tF_{7/2}$ to $(n_t+1)D_{5/2}$, and this in turn causes radiation to build up on that transition until the two populations are equalized. In the case of the $10F$ target, this process was studied in detail [10]. The existence of this maser oscillation, and the resulting population transfer, is responsible for the bright blue visible fluorescence from the target. Similar transitions exist for the other targets, and the existence of similar blue fluorescence suggests that these other maser transitions are also efficiently transferring population to the $(n_t+1)D_{5/2}$ levels. If the linewidth of the maser transition is, in all cases, Doppler limited, then tabulated transition rates [11] indicate that the threshold population for the maser transition should decrease proportional to n_t^{-4}, and that therefore all the high-n targets should be well above threshold for the maser transition. However, a study of the fluorescence spectrum of several targets suggests otherwise. Comparing the fluorescence from the $(n_t+1)D$ state to that from the $6D$ state, a cascade decay product of the n_tF state, leads to the conclusion that, while the $(n_t+1)D$ and n_tF populations are approximately equal for the lower n targets ($n_t<12$), the relative population of the $(n_t+1)D$ state drops by an order of magnitude for $n_t>16$. This would indicate that the efficiency of the population transfer by the maser transition is decreased for the higher-n targets. If this is so, then the target makes a gradual transition from a equal mixture of $n_tF/(n_t+1)D$ to an almost pure n_tF target for $n_t>16$. In either case, the target energy remains very well defined, since the energy difference between n_tF and $(n_t+1)D$ is much less than 0.01 eV for targets with $n>16$. In later comparisons with theory, it will be found that no significant difference is expected between the charge-transfer populations formed with n_tF and $(n_t+1)D$ targets.

The Rydberg-atom target is modulated by chopping the second excitation laser beam. The blue fluorescence from the target is monitored by a photomultiplier tube, using an optical filter which passes only the blue-green fluorescence from the $(n_t+1)D$-$5P$ transitions. The phototube current synchronous with modulation of the target is used to monitor the relative strength of the Rydberg-atom target, and to correct for any short term fluctuations within the period of a particular measurement.

Following the Rydberg-atom target, the beam passes through an electrostatic focusing element which we refer to as the ''repeller.'' It has two primary functions: (1) to remove as much of the primary ion beam as possible while transmitting as much of the charge-transfer beam as possible; and (2) to ionize those highly excited states in the charge-transfer beam which could otherwise be ionized in the Rydberg detector, creating a background signal that would degrade the signal-to-noise in measurements of the RESIS signal. Our repeller is a modified version of a commercial device, the Colutron 400-L decelerator, pictured in Fig. 3, which functions as a double einzel lens. With the aid of the ion-optics program SIMION, it proved possible to find choices of the potentials V_{L1} and V_{L2} which blocked the primary ion beam with only slight loss of the charge transfer beam. Typi-
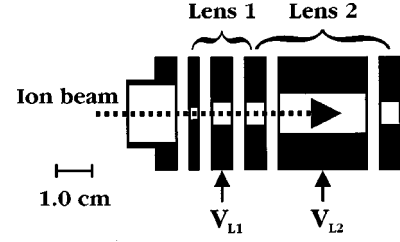
FIG. 3. Geometry of the repeller, to scale. This device, manufactured as a decelerator (Colutron 400-L) is used to discriminate between the primary ion beam and the charge-transfer beam, on the basis of their different energy per charge. It also ionizes very highly excited levels which could produce background in the Rydberg-atom detector.

cally, V_{L2} is set to a voltage slightly greater than the energy per charge of the primary beam. This repels the primary beam but allows transmission of the defocused charge transfer beam. V_{L1} is then adjusted to refocus the charge transfer beam. The second function of the repeller is to reduce the detector background by ionizing highly excited levels. Because the diabatic Stark ionization of the upper state of the RESIS transition takes place over a range of about a factor of 2, it was desireable as having a maximum field in the repeller a factor of 2 larger than the ionizing field in the detector, or at least equal to that field. The maximum field encountered in the repeller, F_R, and the maximum field in the detector, F_D, are both tabulated for each ion in Table II.

A final consideration in the operation of the repeller is the question of its possible effects on the populations which result directly from charge transfer. If the electric fields encountered in the repeller are less than the critical value,

$$E_{\text{mix}} = \frac{q^3}{3n_L^5} \text{ a.u.,} \tag{2}$$

where 1 a.u. of the electric field is 5.1×10^9 V/cm, then there is no possibility of mixing levels with different principal

TABLE II. Settings of the electric fields in the repeller and detector. Column one gives the ion charge. Colum 2 and 3 list the lower and upper levels of the RESIS transition. Column 4 shows the maximum electric field encountered in the repeller lenses, F_R. Column 5 shows the maximum field, F_D, encountered later in the Rydberg detector. Column 6 shows F_{mix}, the repeller field necessary to cause the n_L Stark manifold to overlap with a neighboring n [Eq. (2)]. Column 7 shows the full Stark width of the lower level at the maximum repeller field.

Q	n_L	n_u	F_R (V/cm)	F_D (V/cm)	F_{mix} (V/cm)	$\Delta E_S(n_L)$ (GHz)
2	19	51	1482	1340	5493	990
3	29	71	2142	1204	2238	1500
4	37	85	1434	1390	1569	1860
6	55	133	1439	782	730	2730
8	73	161	2189	864	420	5580
11	102	200	1290	943	205	4680

TABLE III. Details of the several RESIS transitions used in this study. Columns 1–3 identify the ion and its charge and velocity. Column 4 gives the quantum numbers of the lower and upper states of the RESIS transition. Columns 5 and 6 identify the CO_2 laser line used to excite the transition, and column 7 gives the approximate angle of intersection where the resonance was observed. Column 8 gives the observed resonance linewidth, and column 9 lists the values of L which are contained in the high-L peak.

Q	Ion	V (a.u.)	$n_L - n_U$	Line	ν_L	Θ (deg)	W (MHz)	L
1	He^+	0.10	10–30	$10R(20)$	975.930	95.2	60	7–9
2	C^{2+}	0.10	19–51	$9P(20)$	1046.854	110.34	300	9–18
3	C^{3+}	0.10	29–71	$10R(24)$	978.472	96.05	300	13–28
4	C^{4+}	0.10	37–85	$9P(28)$	1039.369	98.30	266	3–36
6	Ne^{6+}	0.10	55–133	$9R(26)$	1082.296	112.94	141	11–54
8	Ar^{8+}	0.10	73–161	$9P(20)$	1046.854	97.82	133	8–72
11	Ar^{11+}	0.10	102–200	$10P(20)$	944.194	98.18	133	7–101
3	Xe^{3+}	0.031	29–71	$10R(24)$	978.472	80.05	375	14–28
3	Ar^{3+}	0.046	31–100	$10P(36)$	929.017	75.72	158	13–30
3	Ar^{3+}	0.057	29–71	$10R(24)$	978.472	83.30	250	13–28
3	C^{3+}	0.081	31–100	$10P(36)$	929.017	79.19	500	11–30
3	C^{3+}	0.130	29–71	$10R(24)$	978.472	85.33	208	13–28

quantum numbers in the repeller since their Stark manifolds do not overlap. For the measurements with ions having $q \leqslant 6$, F_R is less than F_{mix}, and therefore no mixing of populations with nearby n levels can occur. For higher charge states, it was not possible to maintain this condition and still retain-low background. For these cases, there was overlap of Stark manifolds in the repeller. If the anticrossings of these levels are traversed diabatically, as seems very likely, then no exchange of populations would take place. Even in the worst case where such mixing did occur, only levels whose binding energies are within about 10% of the measured level (n_L) could contribute to its population.

Discounting the possible effects of the repeller on the n distribution of the population, there still remains the possibility that the fields encountered in the repeller could change the distribution of product states among the various L states of common n_L. In fact, it seems very likely that the L distribution among the levels contributing to the RESIS high-L peak is completely scrambled in the repeller. To see this, consider that the maximum electric field in the repeller is reached within a time,

$$\Delta t_R \approx \frac{2.0\,\text{mm}}{\nu} = \left(\frac{0.91}{\nu(\text{a.u.})}\right)\,\text{ns}, \tag{3}$$

or about 9 ns, for a typical velocity here. At the maximum field, the typical Stark manifold for the lower state is about 1500 GHz wide (see Table II), but all the fine-structure levels included in the high-L RESIS peak lie within a frequency range at zero field of 500 MHz (see Table III). This means that the time necessary for the Stark width to exceed the zero-field separations of the measured states is much less than 9 ns, approximately 1/3000 times Δt_R, or about 10 ps. Since this is much shorter than 2 ns, the period associated with 500 MHz, the entry into and exit from the repeller fields should be traversed diabatically by the levels contributing to the measured RESIS signals. However, since the relative

phase accumulated by the different Stark levels during their passage through the repeller fields is very large, typically 10^4 cycles, the population of the several L levels should be effectively randomized by the repeller fields. Immediately following the repeller is a set of x-y electric steering plates which can be used to correct for any small deflection of the ion beams by the repeller.

The laser interaction region for this study is of a simple design. A single-frequency CO_2 laser enters from the bottom of the beam pipe through a 2.54-cm-diameter ZnSe window. The laser crosses the beam on its upward path, then is reflected downward from a gold mirror mounted on a rotatable shaft, so that it crosses the beam for a second time at a variable angle. The angle is controlled by a precision rotation stage on which the shaft is mounted. The apparent frequency of the laser beam at its second intersection with the beam is Doppler tuned as the angle of intersection is varied.

$$\nu_L' = \nu_L \frac{(1 + \beta \cos \theta)}{\sqrt{1 - \beta^2}}, \tag{4}$$

where ν_L' and ν_L are the laser frequency in the moving and lab frame, respectively, β is the beam velocity divided by the speed of light, and θ is the intersection angle between the beam and the laser, measured from antiparallel.

The laser is a commercial cw grating tuned CO_2 laser (UltraLaserTech PX2500). The laser shape is TEM_{00}, with a waist size of 0.45 cm and a spot size at the intersection point of about 1.2 cm. The laser power, on the strongest lines, is about 15 W. In order to separate the RESIS signal from backgrounds, the laser is chopped at a frequency of about 510 Hz. There are a wide range of RESIS transitions available in the frequency range of the CO_2 laser. The transitions chosen for this study were at intersection angles close to 90°, where the linewidth due to the 8-mrad angular spread of the ion beam would be minimized. Table III lists the transitions chosen, the laser line used, and the approximate intersection

TABLE IV. Estimated excitation probabilities for the RESIS transitions used in this measurement. The estimates assume a constant linewidth of 200 MHz, a laser power of 10 W, a laser-beam diameter of 1.2 cm, a transit time of 55 ns, and the matrix elements estimated in Eq. (6).

q	n_L	n_U	n_U/n_L	r_{n_L,n_U} (units of a_0)	T_{ex}
1	10	30	3.00	0.49	2.4
2	19	51	2.68	0.31	0.95
3	29	71	2.45	0.25	0.62
4	37	85	2.30	0.22	0.48
6	55	133	2.42	0.13	0.17
8	73	161	2.20	0.12	0.14
11	102	200	1.96	0.12	0.14

angles at resonance. A few additional transitions were studied in order to understand other sources of the linewidth.

Because the upper state of the RESIS transition is very susceptible to Stark broadening, some care was taken to reduce stray electric fields in the laser interaction region. Earth's magnetic field was reduced to less than 50 mG by magnetic shielding. The interior surfaces of the laser interaction region were coated with Aquadag [12], to prevent the buildup of charge on insulating surfaces. In spite of these precautions, clear evidence of Stark broadening by fields on the order of 100 mV/cm was seen when transitions to different upper states were compared in width. It proved possible to reduce these widths by putting a small dc potential on the gold mirror. The observed linewidth was minimized for a potential of about $+0.10$ V on the mirror. We attribute this to differences in the contact potential between the gold mirror surface and the other metal surfaces in the interaction region. The minimum linewidth was about 100 MHz, close to what is expected from the angular collimation of the ion beams. Not all of the measurements are characterized by a linewidth this small.

A rough estimate of the excitation probability on the several RESIS transitions is given by the expression

$$T_{ex} = W(\Delta t) = \frac{4\pi^2}{3}\left(\frac{I}{h\nu}\right)\alpha|r_{n_L n_U}|^2 \nu g(\nu)(\Delta t), \quad (5)$$

where I is the laser intensity in W/m^2, α is the fine-structure constant, ν is the laser frequency, and $g(\nu)$ is the normalized line-shape function. The radial matrix element can be estimated as [13]

$$|\vec{r}_{n_L n_U}|^2 \cong 4\left(\frac{n_L}{n_U}\right)^3\left[1-\left(\frac{n_L}{n_U}\right)^2\right]^{-4}\left(\frac{a_0}{q}\right)^2, \quad (6)$$

Taking the laser power to be 10 W; the linewidth to be 200 MHz, the laser beam diameter to be 1.2 cm, and $\Delta t = 55$ ns, this leads to the estimated excitation probabilities shown in Table IV. For $q=1$, this estimate indicates that the transition is saturated ($T_{ex} > 1$), in agreement with the measurements of Ref. [6]. For larger values of q, this estimate predicts less than an order of magnitude decrease in excita-
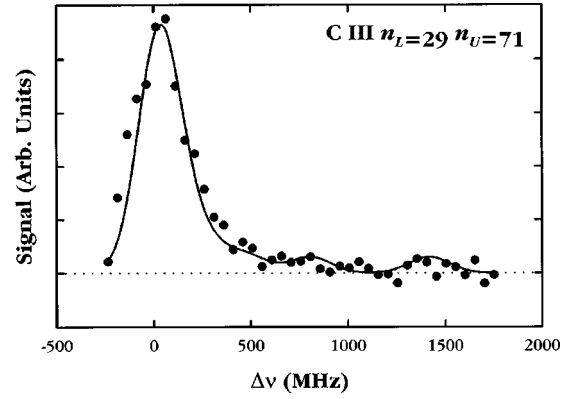
FIG. 4. Typical example of a RESIS excitation signal used in this experiment. This signal is due to excitation of C III (C^{2+} plus a Rydberg electron) from the $n=29$ state to the $n'=71$ level. The horizontal axis plots the difference of the Doppler-tuned laser frequency from the hydrogenic excitation frequency. The large signal near 0 MHz is due to excitation of states with $13 \le L \le 28$. The smooth curve is a simulated signal based on the calculated fine structure of the $n=29$ level. Signals due to excitation of single L states, while suggested by the solid curve, are too small to be resolved. The height of the large peak is taken, in this study, to represent the population of the $n=29$ level.

tion probability up to $q=11$. This is partly due to the choice of stronger transitions as q increases, as indicated by the decreasing ratios of n_U to n_L.

For this study, we will take the unresolved high-L portion of the RESIS signal as an indication of the population of the lower state of the RESIS transition. For example, Fig. 4 shows the 29–71 transition in C III. The strongest line is a superposition of transitions from $n=29$ states with $L = 13-28$. To the right, at higher energies, several resolved peaks are suggested which originate in excitation of single nL states. The range of L states contained in the unresolved peak depends on the excitation linewidth and on the fine structure of the lower state. The fine structure, in turn, is almost entirely due to the polarization energies, which increase the binding of the Rydberg electron over the hydrogenic value by an amount

$$\Delta E = -\frac{e^2}{2}\alpha_d\langle r^{-4}\rangle_{nL}, \quad (7)$$

where α_d is the dipole polarizability of the core ion, and $\langle r^{-4}\rangle_{nL}$ is the hydrogenic radial matrix element. The values of α_d used here for the core ions of this study are listed in Table I. In a few cases there are explicit theoretical predictions. In other cases it was necessary to make estimates. Table I lists the values which have been used, and indicates their source. Given a value of α_d, and a value of the excitation linewidth, the range of L states which contribute to the unresolved high-L peak could be determined. This information is necessary for comparing the measurement results to theoretical predictions. The results of this analysis are listed in Table III.

The final element of the experimental apparatus is the device used to ionize the upper level of the RESIS transition,

and collect the ions that result. It is shown schematically in Fig. 1. It consists of four parts: (1) ionization region, (2) focusing lens, (3) steering and deflection plates, and (4) detection or viewing element.

Diabatic Stark ionization of a Rydberg level takes places abruptly at a critical electric field

$$\frac{q^3}{9n^4} \leqslant F_s(\text{a.u.}) \leqslant \frac{2q^3}{9n^4},$$

where the precise ionization field depends on the other quantum numbers (n_1, n_2, m) of the level. The Stark ionization detector is designed to ionize and ''voltage label'' all Rydberg states of a given value of n. It consists, in principle, of three electrodes along the beam axis, as illustrated in Fig. 1. The first and third electrodes are grounded, and the second is held at a potential V_D. The spacing between the second and third electrodes is d, while that between the first and second is $3d$. The potential V_D is chosen so that the electric field in the smaller gap is sufficient to ionize all atoms with principal quantum number n_u, the upper state of the laser transition:

$$\frac{V_D}{d} = \frac{2q^3}{9n_u^4} \text{ a.u.} \tag{8}$$

Consequently, the electric field in the long gap ($V_D/3d$) will ionize *none* of the states with principal quantum number n_u. Thus all of the atoms in the n_u level ionize immediately upon entry into the second gap. The change in charge which results causes their kinetic energy to either increase or decrease (depending on the sign of V_D) as they return to the ground potential at the third electrode. This change in speed distinguishes the true Stark ionization current from other ions of the same charge that may have been produced in other ways, either residual primary ions which survived passage through the repeller or ions that did capture an electron but then were subsequently collisionally ionized.

In practice, the ionization region consists of two nested sets of electrodes of this type, with a ratio of 3 between their ''small'' gaps. This arrangement makes it possible to detect a much wider range of Rydberg states. With this two region device, values of V_D between 300 and 5000 V can be used to ionize Rydberg states with $20q^{3/4} \leqslant n_u \leqslant 55q^{3/4}$, where q is the charge of the ion core. For this study, an ionizer with a smaller gap ($d = 0.88$ cm) was used for all the signals.

Immediately following the Stark ionizer is a simple aperture lens. This is used to focus the signal beam as tightly as possible in the detector plane. Adjustment of the lens voltage is made possible by real-time viewing of the beam profile on the beam viewing system (Colutron BVS-1) mounted at the end of the detector. Focusing of the RESIS signal directly was very difficult since it is such a small signal. Instead, the signal focus was adjusted by turning off the voltages V_{L1} and V_{L2} in the repeller, and using a target that produces a relatively large population in states near the upper level of the laser transition (typically $n_t = 14$). Under these conditions, there was a large enough Stark-ionized beam so that the focus could be adjusted. Once the optimum focus was deter-

mined, the repeller voltages were turned on again to reduce the background. Since it was also necessary to measure the total charge-transfer beam, a separate choice of optimum lens voltages was made for that beam also [14].

Following the lens, x and y deflection plates were mounted. The x deflection was necessary to compensate for small steering effects of the Stark ionizer. The y deflection was used to separate the several beams emerging from the analyzer by deflecting them vertically from the beam axis. These beams could either be viewed on the BVS-1 viewing system when the deflection was upwards, or directed into a channel electron multiplier (CEM) for quantitative measurement when the beams were deflected downward.

In order to measure the ratio between the RESIS signal and the total charge-transfer beam, it was necessary to switch frequently between detector settings which have been chosen to optimize collection of one or the other of these signals. For this purpose, a single switch was provided to switch between preset values of the voltages in the detector.

MEASUREMENTS

For each choice of incident ion, the first step in the measurement procedure was to obtain a good scan of the high-L RESIS signal. This scan typically consisted of 15–20 measurements at angles scanning the complete high-L resonance. By examination of this resonance scan, three angles were chosen which corresponded approximately to the center of the line, and two angles where the signal has dropped to about half its maximum value. Subsequent measurements of the RESIS signal were made only at these three angles.

Measurement of the ratio between the RESIS signal and the total charge-transfer beam required that each of these quantities be measured separately. With the present detector design, this cannot be done simultaneously. Instead, the detector settings were switched between the settings which gave optimum detection of each type of signal. Both quantities, the RESIS signal and the charge-transfer beam, were measured with the same Channeltron and on the same lock-in amplifier (Stanford Research Systems-830), but not with the same reference signal. For the charge-transfer beam, the reference signal was obtained from a chopper which modulated the second excitation laser of the Rydberg target. The measured lock-in signal in this case corresponds to the charge-transfer beam produced by the Rydberg-atom target, excluding any background charge transfer produced by capture from ground-state Rb or other residual gas in the system. The frequency of this reference signal was 172 Hz. For measurement of the RESIS signal, the reference signal was obtained from a chopper which modulates the CO_2 laser. The frequency of this chopper was 510 Hz. Since the magnitude of the RESIS signal was much smaller than the total charge-transfer beam, the bias voltage on the CEM was different for the two signals, typically 800 V for the charge transfer and 1100 V for the RESIS signal. A separate lock-in amplifier measured the blue fluorescence from the Rydberg target synchronous with the chopping of the second excitation laser.

To make a single measurement of the desired ratio the following sequence of measurements were made.

TABLE V. Typical measurement of the RESIS signal to the charge transfer (CT) signal ratio. This represents one of eight independent data sets taken for the case of C III at $v = 0.10$ a.u. Average CT/Blue, 0.410. The fitted RESIS signal amplitude is 0.0469, and the ratio is 0.114.

Angle	RESIS Sig.	CT Sig.	Blue	(CT)/(Blue)	(RESIS)/(Blue)
— — —	— — —	105.3	242.5	0.4342	— — —
— — —	— — —	102.8	239.6	0.4290	— — —
Θ_1	7.716	— — —	239.4	— — —	0.03223
Θ_1	8.655	— — —	238.6	— — —	0.03627
Θ_2	11.011	— — —	229.9	— — —	0.04789
Θ_2	11.650	— — —	231.2	— — —	0.05039
Θ_3	4.725	— — —	222.2	— — —	0.02126
Θ_3	4.470	— — —	220.8	— — —	0.02024
— — —	— — —	82.7	210.7	0.3925	— — —
— — —	— — —	79.1	205.5	0.3849	— — —

(1) With the detector, lock-in reference, and CEM bias set at the charge-transfer values, the charge-transfer beam and the blue fluorescence were measured twice, with 10 s averaging times.

(2) With the detector, lock-in reference, and CEM bias set at the RESIS values, the RESIS signal at each of the three chosen angles was measured twice, each with an averaging time which varied between 10 and 30 s.

(3) Repeat step (1) to complete data for this ratio measurement.

(4) Remove effects of small fluctuations in the Rydberg target by normalizing the four measurements of charge-transfer [steps (1) and (3)] and the six measurements of the RESIS signal [step (2)] to the simultaneous measurement of the blue fluorescence in each case.

(5) Average the four measurements of normalized charge transfer to obtain a best estimate of the charge transfer.

(6) Fit the six normalized RESIS signal measurements to a Gaussian whose width is fixed at a value found in fitting the detailed signal scan taken earlier. The fitted amplitude is taken to represent the RESIS signal size.

(7) Divide the result in step (6) by the result in step (5). This is the final result for the desired ratio.

A typical example of such a ''data set'' is shown in Table V.

Four data sets like this were taken for a range of Rydberg-atom targets for each choice of incident ion. Then, four additional data sets were taken for the same choices of Rydberg target, but in a different order. The total time necessary for one data set was about 3–9 min, so measurements for one target could be completed in about 30–90 min. For a typical incident ion, about nine different targets were used, meaning that the total measurement time for each incident ion was about 5–15 h. The statistical error on each ratio measurement was taken from the scatter among the eight independent measurements. A typical result for this measured ratio, as a function of the target binding energy, is illustrated in Fig. 5. The results for the other cases are tabulated in Tables VII and VIII and are illustrated in a later figure. As Fig. 5 illustrates, the measured ratio shows a clear variation across the
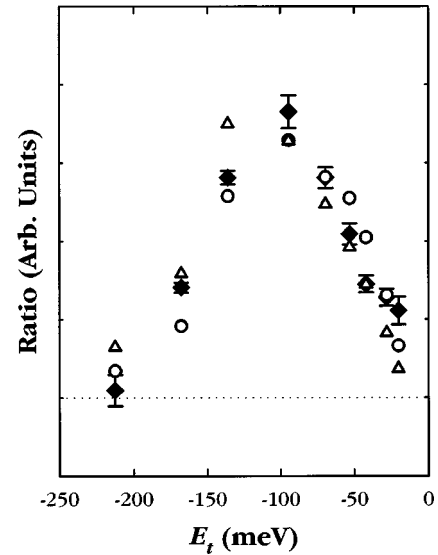
FIG. 5. Typical example of direct comparison between the measured ratio of RESIS signal to charge-transfer beam and CTMC calculations. The solid diamonds represent the measured ratios in the case of $q = 6$ and $v = 0.10$. The measured RESIS signal for this case was the 55–133 transition, and represents the population of the $n = 55$ level with a binding energy of 0.162 eV. The horizontal axis is the binding energy of the several Rydberg-atom targets used in this case. There is a clear variation of the measured ratio across this range of targets. The open triangles show the simplest comparison with the CTMC theory from Eq. (9),

$$R^0_{\text{CTMC}} = \sigma_P / \sigma_T,$$

where σ_p is the calculated cross section for capture into the $n = 55$ level, and σ_T is the calculated total charge-transfer cross section. Since the absolute value of the measured ratios is not significant, the calculated ratios have been adjusted by an overall constant for best agreement with the measurements. While R^0_{CTMC} is in qualitative agreement with the measurements, it is systematically shifted downward. Better agreement is achieved with $R^{\text{corr}}_{\text{CTMC}}$, from Eq. (11) in the text, which is shown by the open circles. This corrected ratio accounts for ionization of part of the charge-transfer beam in the repeller and for the evolution of excited-state populations between the Rydberg-atom target and the CO_2 laser. This example illustrates the relative significance of the various corrections applied to the CTMC calculations. Results for all other cases are shown in Fig. 6.

range of targets used. The relative sensitivity of the charge transfer and RESIS measurements are not known, primarily because both depend on the focusing adjustments in the Rydberg-atom detector. Thus the absolute ratio is uncertain by an unknown factor common to all the measurements for a particular ion. Because of the dependence of the collection efficiency on the detector settings, all the measurements with a given incident ion were made with the same settings of the detector.

COMPARISON WITH CTMC THEORY

The measured ratios can be compared with any theory which predicts both the total charge-transfer cross section and the partial cross section into a particular final level. At

present, only the classical trajectory Monte Carlo method [1] provides such predictions. Quantum methods which have been used to predict charge capture from ground states become impractical because of the very large number of quantum states which could be involved in capture from a Rydberg level. In the CTMC method, the capture process is treated as a classical three-body problem. The initial state of the Rydberg-atom target is represented by a classical orbit, whose size and shape are chosen to be within a discrete range representing its quantum state. In the version of the CTMC method used here [15], the quantum defect of the target state is incorporated by changing the effective charge of the Rb^+ ion core to give the correct binding energy. Once the initial orbit of the target electron is chosen and given a random orientation in space and a random orbital phase. The projectile ion is set in motion with a fixed impact parameter. From this point, the classical equations of motion are integrated to determine the outcome of the collision. After the heavy particles are well separated, if the electron is found to be bound to the projectile ion, then its energy and angular momentum are determined and the corresponding quantum numbers are assigned according to the same discrete correspondence used to set up the initial state. By repeating this calculation for a large number of initial conditions, an estimate can be made of the cross section for capture into any particular quantum level (n,L,m) by any choice of incident ion and Rydberg-atom target.

In its simplest form, the prediction of the CTMC theory for the result of our measurement would be

$$R_{CTMC}^0 = \frac{\sigma_p}{\sigma_T}, \qquad (9)$$

where σ_p denotes the capture cross section into states with principal quantum number n_L and σ_T denotes the total charge transfer cross section. For this and all other CTMC calculations presented here, the Rydberg-atom target is assumed to consist of an equal mixture of $n_t F$ and $(n_t+1)D$ states. Figure 5 illustrates a comparison between this prediction and the measured ratio in a typical case, $q=6$ and $v = 0.10$. The predictions have been adjusted by a common factor to achieve the best agreement with measurements. Even this simple comparison gives reasonably good agreement with the measured ratios.

There are a number of corrections that should be applied to this simple model to achieve the most realistic comparison to the measured ratios. The simplest of these is due to the fact that, since the repeller fields were left on during the measurement of the ''total charge-transfer'' beam, only product states which are not Stark ionized in the repeller should be counted toward the cross section which determines the denominator in the predicted ratio. To account for this, an effective total cross section is defined as

$$\sigma_T' = f_R \sigma_T, \qquad (10)$$

where σ_T' includes only capture to levels with $n \leq n_{cutoff} = (q^3/6F_R)^{1/4}$, where F_R is the maximum electric field in the repeller in a.u. The effect of this factor, f_R, is to reduce the

effective total cross section for the higher n_t targets, since they produce a larger fraction of the population in states that can be Stark ionized in the repeller. The omission of this factor in the report of Ref. [7] was responsible for the apparent disagreement between the measured ratios and the predictions of the CTMC theory noted there.

There are also corrections to the numerator in the calculated ratio. For one thing, not all captures into the n_L level will contribute to the high-L signal, but only a subset of the captures which have appropriate values of L. Knowing the range of L's included in this peak (see Table III), the CTMC calculation will determine ''f_L,'' the fraction of the capture into n_L which is in this subset. Finally, the change in the level populations between the capture at the Rydberg target and the excitation at the CO_2 laser needs to be accounted for. Recall that the distance between the Rydberg-atom target and the repeller is 23 cm, and the distance from the repeller to the CO_2 laser is 22 cm. During both these periods, there will be spontaneous decay, and perhaps blackbody-stimulated transitions which will cause the populations to evolve with time. Fortunately, the lifetimes of the highly excited levels populated in the capture are long compared with the transit times, which are on the order of 1 μs. We can simulate the effects of these spontaneous and stimulated transitions, after assuming the population distributions at the target predicted by the CTMC theory. The result of this calculation is the ratio between the population of the subset of detected levels at the CO_2 laser, and of the same set of levels at the Rydberg target. We denote this calculated ratio as $f_{cascade}$ [16]. Thus we can improve the theoretical estimate of the measured ratio by

$$R_{CTMC}^{corr} = \frac{f_L f_{cascade}\sigma_p}{f_R \sigma_T}, \qquad (11)$$

Figure 5 shows that these improved predictions agree extremely well with the measured values. Again, the predicted values have been adjusted by an overall factor to find the best agreement with the measurements.

Figure 6 shows similar comparisons for all choices of incident ion charge and velocity. For simplicity, only R^{corr} is shown. The results for $q=1$ are taken from Ref. [6]. In general, the comparison shows a remarkable degree of agreement between the measured ratios and the predictions of the CTMC theory. For example in the set of measurements at $v = 0.10$, both the position and width of the measured ratio shift dramatically vs q, but these changes agree extremely well with CTMC predictions. The set of measurements at $q = 3$ shows primarily a variation in the width of the peak as a function of v. Again, the CTMC predictions are in good agreement with this trend. At the two lowest velocities, it appears that the measurements are slightly broader than the predictions, perhaps by 10–20%. At the highest velocity studied, the agreement in shape is not very satisfactory. The reason for this is not known. Still, overall, it is clear that the predictions from the CTMC theory are very close to the observed behavior.

The variation of these measured ratios with n_t combines the variation of σ_P and σ_T. The more interesting of these,
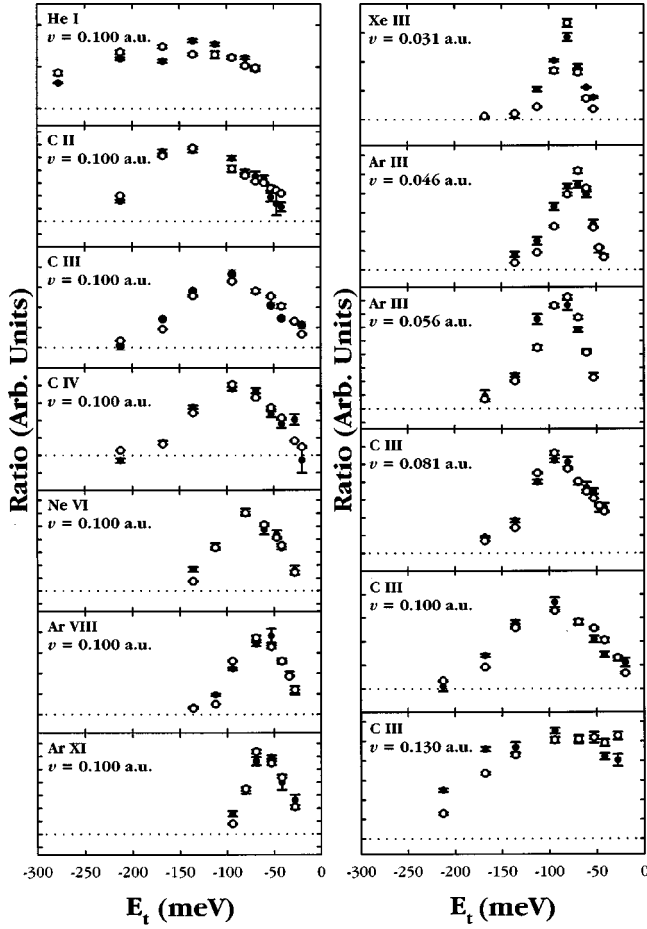
FIG. 6. The measured ratios between RESIS signals and charge-transfer beam for all cases of this study are shown by the solid points. Numerical tabulation of the results is given in Tables VII and VIII. The open circles show $R_{\mathrm{CTMC}}^{\mathrm{corr}}$, from Eq. (11) in the text, adjusted by a constant factor in each case. The shape and position of the ratio curve varies widely with the charge and velocity of the projectile ion, but the agreement with the predictions of the CTMC theory is generally good throughout. The poorest agreement is seen for the lowest velocities at $q=3$ ($v=0.031$ and 0.046), where the measurements appear slightly wider than the predictions, and at the highest velocity at $q=3$ ($v=0.130$), where there appears to be disagreement in the position of the curve.

σ_P, gives the cross section into a fixed energy product state from initial states of various energies. This is a quantity which is analogous to the partial cross sections into various final states from a fixed initial state. We can obtain an estimate of σ_P from the measured ratios by multiplying by the value of σ_T calculated with the CTMC theory. More precisely, including several correction factors,

$$\sigma_p \cong \frac{f_R \sigma_T}{f_L f_{\mathrm{cascade}}} R_{\mathrm{measured}}. \tag{12}$$

Figure 7 shows the values of σ_P which result from this estimate. To within the precision of the measurements, these measurements appear to conform to relatively simple resonance curves. This provides a way to parametrize the results,
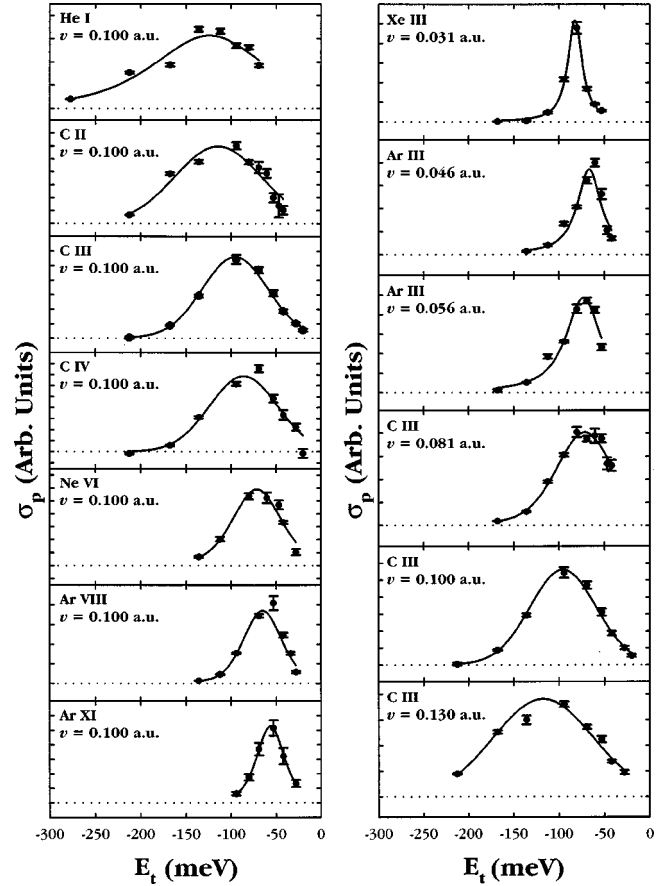
FIG. 7. Estimates of the partial cross section for capture into a final level of fixed energy (E_p) from initial Rydberg targets of varying energy (E_t). These are obtained from the measured ratios (see Fig. 6 and Tables VII and VIII), by multiplying by the calculated total cross section, as in Eq. (12) of the text. The solid curves are fits to the resonance shape of Eq. (13), which are used to parametrize the curves in terms of the center energy E_t^{max} and the full width at half maximum W. Because the energy of the detected level, E_p, varies slightly from case to case, E_t^{max} is measured in terms of E_p and defined by the parameter $\kappa \equiv E_t^{\mathrm{max}}/E_p$. The fitted parameters κ and W are shown in Table VI, along with parameters obtained in similar fits of direct CTMC calculations of σ_p.

by fitting to such a curve and extracting the position and width of the curve. Most of the results can be well fit by a simple Gaussian. However, the results at the lowest velocities are much better fit by a Lorentzian. We chose to fit them to the following function, which incorporates both Gaussian and Lorentzian curves as special limits:

$$\sigma_p(E_t, E_p) = A \left\{ c \left[\frac{1}{1 + 4\left(\dfrac{E_t - \kappa E_p}{W}\right)^2} \right] + (1-c) \right.$$

$$\left. \times \left[e^{-277[(E_t - \kappa E_p)/W]^2} \right] \right\}. \tag{13}$$

Here κE_p is the value of E_t at the peak cross section, W is the full width at half maximum of the curve, and c deter-

TABLE VI. Best-fit values of the parameters κ and W from fits of the measured σ_p's, and from fits of CTMC calculations of σ_p. The value of χ^2 per degree of freedom (DOF) for each fit is also shown. The fact that these are consistently greater than 1 indicates that the fitting function is not quite correct.

q	v (a.u.)	Expt.			CTMC		
		κ	W	χ^2 (DOF)	κ	W (eV)	χ^2 (DOF)
1	0.10	0.91(5)	0.15(3)	31.1	0.97(2)	0.193(2)	3.6
2	0.10	0.76(3)	0.113(15)	13.7	0.759(10)	0.118(8)	20.1
3	0.10	0.658(6)	0.086(4)	2.1	0.635(13)	0.093(5)	64.7
4	0.10	0.54(2)	0.089(8)	11.5	0.54(2)	0.077(7)	555.3
6	0.10	0.442(14)	0.064(8)	6.1	0.436(12)	0.064(5)	45.3
8	0.10	0.400(9)	0.051(4)	16.5	0.396(8)	0.046(4)	105.4
11	0.10	0.357(7)	0.037(4)	0.1	0.359(4)	0.038(3)	12.3
3	0.031	0.566(8)	0.019(5)	12.9	0.567(2)	0.0169(6)	29.3
3	0.046	0.524(15)	0.032(7)	18.3	0.518(12)	0.025(6)	341.0
3	0.057	0.503(14)	0.047(8)	14.6	0.516(6)	0.039(4)	145.0
3	0.081	0.562(14)	0.075(4)	3.6	0.572(13)	0.078(5)	130.7
3	0.130	0.809(14)	0.130(12)	7.2	0.717(8)	0.129(7)	12.5

mines the Gaussian and Lorentzian character of the curve. The best fit values of κ and W are given in Table VI. Also shown in Table VI are the results of similar fits of the direct predictions of σ_p by the CTMC theory. The fitted values of κ and W from theory and experiment are in good agreement. The fitted values of c are of less interest. Generally c was small, indicating a Gaussian shape, except at the lowest velocities where it was near 1, indicating a Lorentzian shape. This behavior was seen both in the measured σ_p's and in the CTMC calculation. Table VI also gives values of χ^2 per degree of freedom for each fit. The fact that these values are consistently greater than 1 indicates that the fitting function does not reproduce the data within the stated errors. The errors in the fitted parameters were expanded to account for the poor fit, but because of the poor fit, they should be viewed with some caution.

Figure 8 illustrates the fitted values of κ, plotting $1/\kappa$ vs q for the measurements at $v = 0.10$ a.u. Since $1/\kappa = E_p/E_t^{\max}$, this plot illustrates the degree to which the product state tends to be more tightly bound than the target state. Note that the measurements are completely consistent with the predictions of the CTMC theory, which are shown in the figure by the open squares. The measurements are similar in shape to the function predicted by the overbarrier model [17],

$$\frac{E_p}{E_t} = \frac{q + 2\sqrt{q}}{1 + 2\sqrt{q}}, \tag{14}$$

but clearly inconsistent with this prediction. Similarly, they are inconsistent with the simple anzatz suggested some time ago by examination of CTMC results [1]:

$$\frac{E_p}{E_t} = \sqrt{q}. \tag{15}$$

Both these convenient and often cited analytic expressions are illustrated in Fig. 8, where their inconsistency with the present measurements can be clearly seen. A figure similar to

Fig. 8 was reported in Ref. [7], and showed disagreement between measurements and CTMC predictions. This apparent disagreement is due to the neglect, in Ref. [7], of the correction factor f_R. Recall that f_R represents fraction of the charge-transfer beam which is transmitted through the repeller. This decreases as the target binding energy decreases, since a larger fraction of the charge-transfer beam is in very highly excited states which can be ionized in the repeller. Neglect of this factor would shift the curves representing σ_p
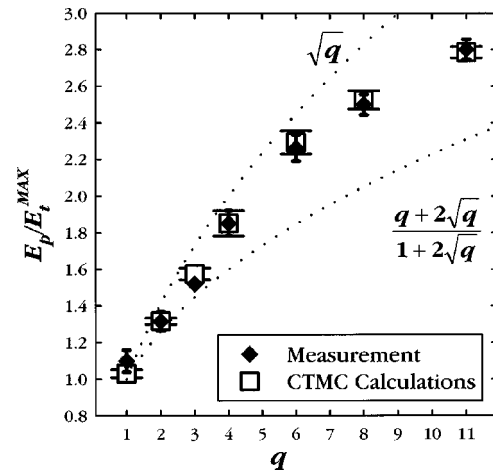
FIG. 8. Fitted values of $E_p/E_t^{\max}$ for capture by ions with $v = 0.10$ a.u. and $1 \leq q \leq 11$. The plotted value is κ^{-1}, where κ is the parameter obtained in fits of the partial cross sections (Fig. 7). The dotted curves show two widely used predictions. The lower curve shows the function predicted by the classical overbarrier model. The upper curve shows an empirical estimate obtained by inspection of CTMC predictions. Neither of these formulas is in satisfactory agreement with the measured values. The open squares, however, are obtained by fitting explicit CTMC predictions for the partial cross sections analogous to the measured values to the same functional form used for the measurements. These are in excellent agreement with the measurements for all charges.
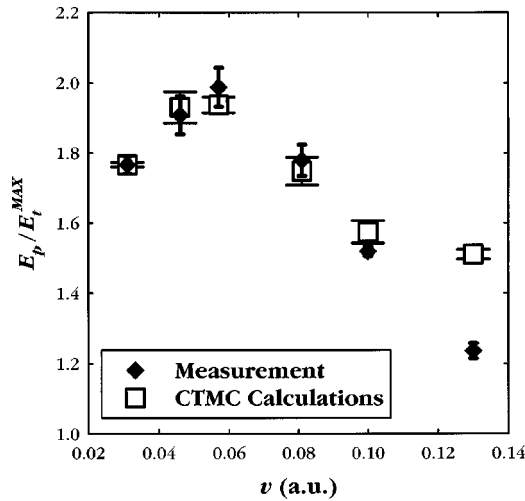
FIG. 9. Fitted values of $E_p/E_t^{\max}$ for capture by ions with $q = 3$ and various velocities. The horizontal axis is the ion velocity in atomic units where 1 a.u. $= \alpha c$, with α the fine structure constant and c the speed of light. As in Fig. 8, the plotted values are simply κ^{-1}, where κ is the parameter obtained in fits of the measured partial cross sections. The observed behavior is in contrast to that expected from the level-crossing model of the charge-transfer reaction, which would predict a smooth 10% increase across this range of velocities. The open squares show the results obtained from CTMC calculations of the specific partial cross sections analogous to the measurements.

to the right in Fig. 7, and result in an overestimate of the factor $1/\kappa$.

The variation of $1/\kappa$ with velocity is illustrated in Fig. 9.
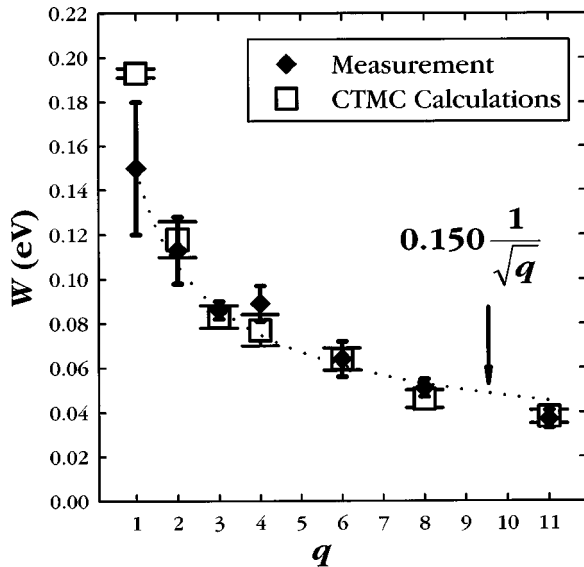
FIG. 10. Fitted values of the parameter W, measuring the full width at half maximum of the partial cross section measurements of Fig. 7. These results are for ions with $v = 0.10$ a.u. and $1 \le q \le 11$. The dotted curve shows that the results are consistent with a $q^{-1/2}$ dependence over this range. The open squares show the results of a similar fit of explicit CTMC predictions of the partial cross sections. These are in very good agreement with the measurements.
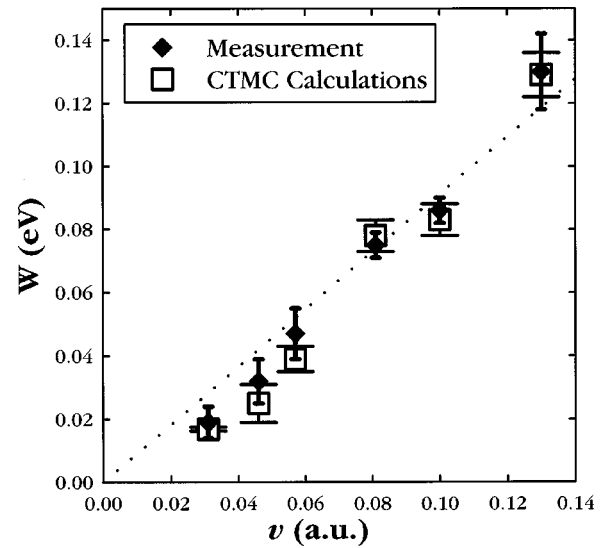
FIG. 11. Fitted values of the parameter W, measuring the full width at half maximum of the partial cross section curves, for ions of charge 3 and various velocities. The measured results are consistent with the dotted curve which is proportional to the velocity. The open squares show the results of fitting explicit CTMC predictions of the relevant partial cross sections.

The measured values are again in good agreement with the predictions of the CTMC theory, with the possible exception of the highest velocity point. The nonmonotonic behavior indicates that the ratio of binding energies of the product state and the target state does not increase monotonically with velocity, as has been predicted by considerations of the ''reaction window'' in a level crossing picture of the charge capture reaction [18]. Over this range of velocities the reaction window picture would predict a smooth 10% increase in $1/\kappa$, which is clearly different from the observed behavior.

Figure 10 shows the fitted widths for the σ_p curves at fixed $v = 0.10$. These are seen to decrease with q, approximately as

$$W(\nu = 0.10 \, \text{a.u.}) \cong \frac{0.15 \ \text{eV}}{\sqrt{q}}, \tag{16}$$

which is represented by the dashed line in Fig. 10. We know of no simple explanation for this dependence on q.

It is interesting to note that the analogous width in the product space changes very little with q, if the predictions of the CTMC theory are accurate. This difference is suggested by the functional form of our fitting function [Eq. (13)]. In this expression, W is the full width at half maximum in the variable E_t, but the width in the variable E_p is W/κ. Since $1/\kappa$ is approximately $q^{1/2}$, this suggests that the width in the product space (E_p) is greater than in the target space (E_t) by about $q^{1/2}$. This implies an approximately constant energy width in the product space for the several values of q studied, and this is exactly what is seen in CTMC predictions.

The variation of the width of the σ_p curve as a function of velocity, at fixed $q = 3$ is illustrated by Fig. 11. The measured values are consistent with a purely linear dependence, represented by

TABLE VII. Measured ratios between the amplitude of the high-L RESIS signal and the total charge-transfer beam (in arbitrary units) for ions of varying charges and constant velocity of $v = 0.10$ a.u. The quoted errors are one standard deviation estimates based on the scatter between at least eight independent measurements. Column 1 gives the principal quantum number n_t of the $F_{7/2}$ state excited to form the Rydberg-atom target.

n_t	$q=1$	$q=2$	$q=3$	$q=4$	$q=6$	$q=8$	$q=11$
7	0.721(18)	– – –	– – –	– – –	– – –	– – –	– – –
8	1.363(35)	0.032(2)	0.02(4)	−0.015(6)	– – –	– – –	– – –
9	1.550(41)	0.110(3)	0.282(12)	0.037(5)	– – –	– – –	– – –
10	1.765(40)	0.111(3)	0.562(18)	0.138(5)	0.084(9)	0.036(2)	– – –
11	1.640(43)	– – –	– – –	– – –	0.172(13)	0.095(6)	– – –
12	1.283(33)	0.099(3)	0.73(4)	0.191(5)	– – –)	0.222(6)	0.0079(10)
13	1.225(33)	0.079(2)	– – –	– – –	0.304(14)	– – –	0.0168(12)
14	0.918(29)	0.071(7)	0.56(3)	0.186(8)	– – –	0.341(9)	0.0281(16)
15	– – –	0.066(6)	– – –	– – –	0.238(19)	– – –	– – –
16	– – –	0.038(7)	0.42(3)	0.119(8)	– – –	0.38(3)	0.0297(7)
17	– – –	0.028(18)	– – –	– – –	0.219(16)	– – –	– – –
18	– – –	0.022(7)	0.29(2)	0.090(12)	0.166(5)	0.260(12)	0.020(3)
20	– – –	– – –	– – –	– – –	– – –	0.199(9)	– – –
22	– – –		0.26(2)	0.103(15)	0.081(18)	0.108(11)	0.013(2)
26	– – –	– – –	0.22(4)	−0.014(36)	– – –	– – –	– – –

$$W(q=3) = 0.90\nu \text{(a.u.)}, \tag{17}$$

Again, the measured values are in full agreement with the predictions of the CTMC theory. The linear dependence on velocity is inconsistent with the $\sqrt{\nu}$ dependence predicted in one version of the overbarrier model [19].

DISCUSSION

This experiment represents by far the most extensive and quantitative study of energy transfer in charge exchange by slow ions on highly excited atoms. Previous studies were confined to singly charged ions over a range of velocities [2] or to ions of charge $q=8$ at two velocities [3]. In contrast, this study included a wide range of charges and velocities. The previous studies used selective field ionization to analyze the final-state distribution after charge transfer, and both revealed an apparent disagreement with the details predicted by the CTMC theory. In contrast, this study uses lasers to fully define the energy of both initial and final states, and finds virtually complete agreement with the predictions of the CTMC method. The range of validity of the CTMC method at low velocities is difficult to assess in the absence of experiments or other computational methods [20]. It has often been assumed that the limit of validity is $\nu = \nu_e$, or reduced velocity$=1$ [1]. This study extends to reduced velocities as low as 0.3, with no sign of disagreement. Other recent experiments have also suggested that CTMC predictions could be valid well below a reduced velocity of 1 [21]. Perhaps the simplest conclusion that can be drawn from this study is that, to within the precision of this measurement and over the range of parameters included, the description of ion–Rydberg-atom charge transfer by the classical CTMC theory appears to be completely satisfactory. If there is a significant breakdown of the CTMC theory at low velocities, as has been suggested, it occurs beyond the range of the present experiment. In contrast, the quantitative measurements of this study are clearly inconsistent with some of the clear predictions of the overbarrier and level-crossing pictures of the charge-capture process.

It is true that the poorest agreement with the CTMC theory observed in this experiment is at the lowest velocities, where the observed $q=3$ resonances are slightly wider than predicted, and at the highest velocity, where there appears to be a disagreement in shape. This suggests that further studies at the extreme velocities should be pursued. It would be interesting to know if the apparent disagreement at $\nu = 0.130$ for $q=3$ would be confirmed by a remeasurement, and if it persists at even higher velocities. Even more interesting, though, would be extensions of these measurements to lower velocities. There are a number of reasons to expect that the CTMC theory cannot continue to be valid at extremely low velocities. Some have suggested that the onset of tunneling will become dominant at low enough velocities, making the classical picture fail [22]. Others expect that the increasing importance of quasimolecular effects will make the simple classical model fail [21]. We can already see from the widths measured here that quantum discreteness of the allowed energy levels must become a factor only at slightly lower velocities. For all of these reasons, measurements at even lower projectile velocities would be the most interesting extension of this measurement. Previous studies of the total charge-exchange cross section in a region of reduced velocity below 1 have revealed cross-section oscillations which correlate with multiple ''swapping'' of the captured electron between the projectile and core [21]. This behavior suggests the onset of moleculelike behavior, which is expected to dominate the extremely low-velocity behavior of charge exchange.

TABLE VIII. Measured ratios between the amplitude of the high-L RESIS signal and the total charge-transfer beam (in arbitrary units) for ions of varying velocity (in atomic units) and constant charge $q=3$. The quoted errors are one standard deviation estimates based on the scatter between at least eight independent measurements. Column 1 gives the principal quantum number n_t of the $F_{7/2}$ state excited to form the Rydberg-atom target.

n_t	$v=0.031$	$v=0.046$	$v=0.057$	$v=0.081$	$v=0.100$	$v=0.130$
8	– – –	– – –	– – –	– – –	0.02(4)	0.250(8)
9	0.009(2)	– – –	0.019(8)	0.046(3)	0.282(12)	0.459(11)
10	0.013(7)	0.16(3)	0.049(2)	0.091(5)	0.562(18)	0.46(3)
11	0.105(7)	0.30(4)	0.132(7)	0.201(6)	– – –	– – –
12	0.205(4)	0.66(4)	0.152(3)	0.261(6)	0.73(4)	0.553(15)
13	0.286(13)	0.87(3)	0.153(7)	0.257(14)	– – –	– – –
14	0.185(7)	0.89(4)	0.116(3)	0.198(6)	0.56(3)	0.511(14)
15	0.111(2)	0.79(3)	0.084(3)	0.185(15)	– – –	– – –
16	0.076(3)	0.48(4)	0.049(3)	0.174(8)	0.42(3)	0.52(3)
17	– – –	0.21(3)	– – –	0.127(12)	– – –	– – –
18	– – –	0.146(16)	– – –	0.129(12)	0.29(2)	0.422(16)
22	– – –	– – –	– – –	– – –	0.26(2)	0.40(3)
26	– – –	– – –	– – –	– – –	0.22(4)	– – –

Whether, and how, the swapping phenomenon is reflected in the energy distributions of captured electrons is yet to be explored.

Another direction that holds promise for future studies of the ion–Rydberg-atom charge transfer by the RESIS technique is the more detailed analysis of final state distributions. The L distributions in final states of neutral Rydberg atoms were studied by the RESIS method in Ref. [5]. Similar studies should be possible for $q>1$, although these will require a higher signal-to-noise ratio than was obtained for the present measurement.

An intriguing application of the Rydberg-atom target used here might be as a source of controlled initial population of highly excited ions in other studies. Now that the energy distribution functions have been characterized experimentally, they could be used as a way to create initial populations of well-controlled binding energies. It might even be possible to populate highly excited ion states with completely well-determined principal quantum numbers by this technique.

APPENDIX

In Tables VII and VIII we present ratios between the amplitude of the RESIS signal and the total charge-transfer beam.

[1] R. E. Olson, J. Phys. B **13**, 483 (1980).

[2] K. B. MacAdam, L. G. Gray, and R. G. Rolfes, Phys. Rev. A **42**, 5269 (1990).

[3] A. Pesnelle *et al.*, Phys. Rev. A **54**, 4051 (1996).

[4] Thomas F. Gallagher, *Rydberg Atoms* (Cambridge University Press, Cambridge, 1994), pp. 103–115.

[5] F. J. Deck, E. A. Hessels, and S. R. Lundeen, Phys. Rev. A **48**, 4400 (1993).

[6] D. S. Fisher *et al.*, Phys. Rev. A **56**, 4656 (1997).

[7] D. S. Fisher *et al.*, Phys. Rev. Lett. **81**, 1817 (1998).

[8] Martin P. Stockli *et al.*, Rev. Sci. Instrum. **63**, 2822 (1992).

[9] B. D. DePaola *et al.*, Phys. Rev. A **52**, 2136 (1995).

[10] C. W. Fehrenbach, S. R. Lundeen, and O. L. Weaver, Phys. Rev. A **51**, R910 (1995).

[11] Anders Lindgard and Svend Erik Nielson, At. Data **19**, 533 (1977).

[12] Acheson Colloids Co., Port Huron, MI.

[13] Hans A. Bethe and Edwin Salpeter, *Quantum Mechanics of One and Two-Electron Atoms* (Springer-Verlag, Berlin, 1957). Our Eq. (6) is obtained from Eq. 63.11 of this reference. It represents an average over all the states in the n and n' levels.

[14] D. S. Fisher, Ph.D. thesis, Colorado State University, 2000.

[15] M. Karplus, R. N. Porter, and R. D. Sharma, J. Chem. Phys. **43**, 3259 (1965).

[16] One ambiguity in calculating $f_{cascade}$ is the effect of the electric fields in the repeller on the populations in the Rydberg-atom beam. As discussed above, mixing between different n levels is unlikely, but mixing between the several unresolved L states in the high-L RESIS signal seems certain. Mixing with lower L states which are not contained in this peak is questionable, and depends on the quantum defects of those levels. We calculated

f_{cascade} in the two extreme cases of (a) no mixing between any of the level populations in the repeller, and (b) complete randomization of the populations of the several L levels within each n. While the absolute value of f_{cascade} differed in the two cases, there was no significant change in the dependence on the target energy. We used the average of these two calculations to process the data, and concluded that uncertainty about the exact effect of the repeller fields does not affect our conclusions.

[17] V. N. Ostrovsky, J. Phys. B **28**, 3901 (1995).

[18] Knud Taulbjerg, J. Phys. B **19**, L367 (1986).

[19] A. Niehaus, J. Phys. B **19**, 2925 (1986).

[20] J. Pascale, R. E. Olson, and C. O. Reinhold, Phys. Rev. A **42**, 5305 (1990).

[21] K. B. MacAdam *et al.*, Phys. Rev. Lett. **75**, 1723 (1995).

[22] D. Banks, K. S. Barnes, and J. McB. Wilson, J. Phys. B **9**, L141 (1976).

[23] A. Dalgarno and J. T. Lewis, Proc. R. Soc. London, Sec. A **233**, 70 (1955).

[24] C. F. Fischer (private communication).

[25] A. K. Bhatia and Richard J. Drachman, Phys. Rev. A **59**, 205 (1999).